

FINet: Dual Branches Feature Interaction for Partial-to-Partial Point Cloud Registration

Hao Xu^{1,2} Nianjin Ye² Shuaicheng Liu^{1,2} Guanghui Liu¹ Bing Zeng¹

¹University of Electronic Science and Technology of China

{xuhao02@std., liushuaicheng@, guanghuiliu@, eezeng@}uestc.edu.cn

²Megvii Technology

{xuhao02, yenianjin, liushuaicheng}@megvii.com

Abstract

Data association is important in the point cloud registration. In this work, we propose to solve the partial-to-partial registration from a new perspective, by introducing feature interactions between the source and the reference clouds at the feature extraction stage, such that the registration can be realized without the explicit mask estimation or attentions for the overlapping detection as adopted previously. Specifically, we present FINet, a feature interaction-based structure with the capability to enable and strengthen the information associating between the inputs at multiple stages. To achieve this, we first split the features into two components, one for the rotation and one for the translation, based on the fact that they belong to different solution spaces, yielding a dual branches structure. Second, we insert several interaction modules at the feature extractor for the data association. Third, we propose a transformation sensitivity loss to obtain rotation-attentive and translation-attentive features. Experiments demonstrate that our method performs higher precision and robustness compared to the state-of-the-art traditional and learning-based methods.

1 Introduction

Point cloud registration is a longstanding research problem in the areas of computer vision and computer graphics, including augmented reality [1, 2, 3], object pose estimation [4, 5] and 3D reconstruction [6, 7]. It aims to predict a rigid 3D transformation, aligning the source point cloud to the reference. Data association is important, sometimes even critical, for aligning two point clouds, especially for the practical partial-to-partial registrations where inputs are obscured by partiality and contaminated by noise. Algorithms for this task have been improved steadily, which can be divided into two categories: correspondence matching-based methods and global feature-based methods.

Iterative Closest Point (ICP) [8] is the most classical algorithm for the correspondence matching-based methods, where the correspondences are obtained by the nearest neighbor search and the rigid transformation is solved by singular value decomposition (SVD). Subsequently, several methods [9, 10, 11, 12, 13, 14] are proposed to either improve the matching quality or search a larger motion space. Recently, several learning-based approaches [15, 16, 17, 18, 19] replace the handcrafted feature descriptor with neural network to improve the robustness and performance. Specifically, Wang *et al.* [16] adopts graph neural network (GNN) [20] and attention mechanism [21] to refine the point-wise features, which enables the information exchange between the inputs. However, all of them rely on the 3D feature points that extracted base on the local geometric structures. As a result, they can not utilize the geometric knowledge of the entire point clouds. Without a global picture, the data association is inefficient.

In contrast, global feature-based methods can overcome the above-mentioned issues by aggregating global features from point-wise features without correspondences, e.g., PointNetLK [22] and Feature-metric Registration (FMR) [23]. Although they can learn deep features from the entire point cloud, all of them lack of the data association, resulting in poor performances for the partial-to-partial registration. Recently, OMNet [24] predicted overlapping masks, converting the partial-to-partial registration to the registration of the same shape. However, the mask is predicted based on the deep features that extracted without early information exchange, making the masks harder to be estimated accurately, so that to further influence the registration quality.

In this paper, we propose to solve the partial-to-partial registration from a new perspective, by introducing feature interactions between the input source and reference point clouds. We show that abundant information exchange between inputs at the feature extraction stage can naturally equip the network with the capability of partiality perceptions. As such, the global features from the two input clouds can focus on the same parts of an object. Interestingly, this can be achieved implicitly without the need of explicit mask estimations or attention modules, as long as feature interactions are enabled.

To this end, we propose FINet: a feature interaction-based structure with the ability to enable and strengthen the data association between the inputs at multiple stages. To promote the information associating between the inputs, several interaction modules are inserted to the feature extractor. On the other hand, the 3D rigid transformation consists of 3D translation and 3D rotation, which resides in the different solution spaces. Previously, they are regressed from the same deep feature. In this work, we implement a dual branches structure to process the translation and the rotation features separately so as to enhance the concentration of interactions. Moreover, based on the dual branches structure, we propose a transformation sensitivity loss, which encourages the network to extract the rotation-attentive and translation-attentive features, improving the quality of regression from their own solution space. Furthermore, to avoid the issue that the network concentrates on the local geometry, we further propose a point-wise feature dropout loss to encourage aggregating the features globally from different places instead of locally. Experiments show that our approach achieves state-of-the-art performance compared with the previous algorithms.

We summarize our key contributions as follows:

- We propose a multi-level feature interaction structure for the point cloud registration, which promotes the information association between the source and the reference inputs, enabling a better partial cloud perception of the feature extraction.
- We propose a dual branches structure, which can alleviate the affect of solution space difference between the rotation and translation, so as to further enhance the feature interactions.
- We design a transformation sensitivity loss, which supervises the feature extractors of two branches to learn rotation-attentive and translation-attentive features accordingly. In addition, we propose a point-wise feature dropout loss to promote the learning of global information.
- We provide qualitative and quantitative comparisons under clean, noisy, and different partially visible datasets, showing the state-of-the-art performance.

2 Related Work

Correspondence Matching-based Methods. The best-known ICP [8] and its variants [9, 10, 11, 12, 13] are the earlier correspondence matching-based methods, which calculate the nearest neighbors as correspondences. However, they are often strapped into local minima due to the non-convexity. To this end, Go-ICP [14] utilizes a branch-and-bound strategy to find a good optimum at the expense of speed. Furthermore, Fast Global Registration (FGR) [25] uses FPFH [26] features and an alternating optimization technique to further improve efficiency. Recent learning-based methods use Multi-Layer Perceptron (MLP) based network [27, 28] or GNN [20] to replace the handcrafted feature descriptor. Specifically, DCP [15] calculates feature-to-feature correspondences. 3D-FeatNet [29] and USIP [30] learn to detect salient keypoints.

Generally, the accurate matching and the salient keypoints detecting heavily rely on the distinctive geometric structures. However, not all regions are distinctive, which limits the number of correspondences or keypoints, and may cause poor distribution. Moreover, the features of matched points are calculated only from the local geometry, leaving the rest of the points untouched. In addition, an extra RANSAC [31] process may be needed, which is time-consuming. In contrast, our work can adaptively aggregate information from the entire point clouds and achieve an end-to-end registration.

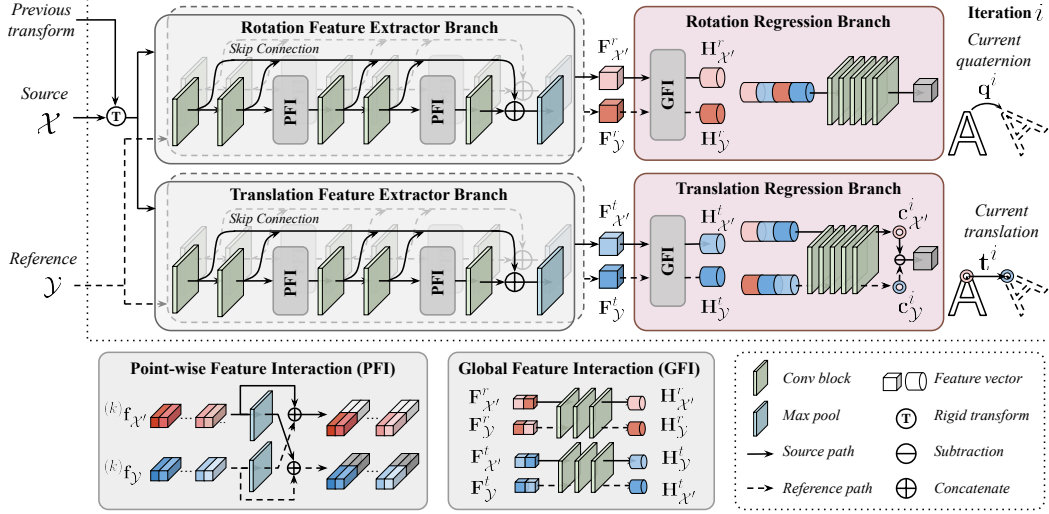


Figure 1: Network architecture for FNet and the multi-levels feature interaction modules.

Global Feature-based Methods. To take the global geometry into consideration, global feature-based methods compute rigid transformation from the entire point clouds. PointNetLK [22] pioneers these methods, which utilizes the Lucas & Kanade (LK) algorithm [32] after PointNet [27] to solve the rigid transformation. PCRNNet [33] improves the robustness to noise by replacing the LK algorithm with a MLP. Subsequently, FMR [23] constrains the global feature distance of the inputs with an extra decoder. However, all of them ignore the effect of partiality. Our network is aware of the partiality and performs well with different partial manners.

Partial-to-partial Registration. As a more realistic problem, partial-to-partial registration is studied by several recent works [16, 17, 18, 24]. In particular, PRNet [16] extends DCP [15] to an iterative variant, and using the Gumble-Softmax [34] to improve the feature matching ability. Following a similar idea, RPMNet [17] uses a small CNN to predict the parameters of the Gumble-Softmax, and the Sinkhorn normalization [35] is further applied to encourage the bijectivity of the matching result. In addition, OMNet [24] handles the partiality by predicting overlapping masks to avoid the effect of outliers. Nevertheless, these methods lack early information exchange or even the data association between the inputs during the feature extraction, resulting in partiality-imperceptible features. In contrast, our method designs specific structures to consider the data association.

Feature Interaction. Some of the previous works implement the data association during the feature extraction. Particularly, DCP [15] borrows the attention module from [21] to enable information exchanging between the inputs. Similarly, PRNet [16] applies DCP iteratively and inserts keypoints detection before it. However, the 3D feature points of them calculated only from the local geometry, resulting in the lack of global information, further reducing the effectiveness of the feature interaction. Besides, the data associations in OMNet [24] is located after the point-wise feature extractor, which is too late to catch enough partiality knowledge. However, our method possesses feature interactions at multiple levels, which enables the partiality perceptual ability.

3 Method

Figure 1 shows an illustration of our method. We estimate the 3D rigid transformation iteratively, which is represented in the form of quaternion \mathbf{q} and translation \mathbf{t} . The entire structure can be divided into two parts: a dual branches encoder (§C.1) and a dual branches transformation regressor (§C.2), where the multi-level features of the source and the reference point clouds are interactive with each other (§3.4). Finally, the loss functions are detailed explained (§3.5).

3.1 Notation

Here we introduce some notation that will be used throughout the paper. The registration problem is that for a given source point cloud $\mathcal{X} \in \mathbb{R}^{3 \times N_{\mathcal{X}}}$ of $N_{\mathcal{X}}$ points and a reference point cloud $\mathcal{Y} \in \mathbb{R}^{3 \times N_{\mathcal{Y}}}$ of $N_{\mathcal{Y}}$ points, we aim to find the ground truth 3D rigid transformation $\{\mathbf{R}, \mathbf{t}\}$ that aligns \mathcal{X} to \mathcal{Y} .

3.2 Dual Branches Encoder

Since the translation belongs to Euclidean space, which is little correlated to the quaternion space. It is not appropriate to obtain the rotation-attentive and translation-attentive features with shared weights. Meanwhile, the features that only contain the rotation or translation information are more beneficial to the data association. To this end, we use a dual branches encoder to extract features for them separately. Refer to [36], point-wise features that output from each convolution block in the MLP are extracted to combine the multi-level features by max-pooling. To promote the low-level information propagation between the source and the reference point clouds, two point-wise feature interaction modules are injected into the encoder. At each iteration, the source point cloud \mathcal{X} is first transformed by the previous transformation into the transformed point cloud \mathcal{X}' . The encoder takes \mathcal{X}' and the reference point cloud \mathcal{Y} as inputs, generating the global features as follow:

$$\mathbf{F}_m^n = \max(\text{cat}[\{\mathbf{f}_m^{(k)} | k = 1..K\}]) \quad \text{where} \quad m \in \{\mathcal{X}', \mathcal{Y}\}, n \in \{r, t\}. \quad (1)$$

Here, the superscript r and t denote the global features \mathbf{F} that belong to the rotation and the translation encoders respectively. The superscript k represents the point-wise features \mathbf{f} that output from the k -th convolution block, and there are K blocks in total. $\max(\cdot)$ denotes channel-wise max-pooling, and $\text{cat}[\cdot, \cdot]$ means concatenation. Note that the encoder is shared weights for the input \mathcal{X}' and \mathcal{Y} .

3.3 Dual Branches Regression

Given the distinctive features \mathbf{F}^r and \mathbf{F}^t of the inputs, we use a global feature interaction module to fuse them, which produces the hybrid features \mathbf{H}^r and \mathbf{H}^t for the rotation and the translation respectively. Consistent with the encoder, a dual branches regression network is applied to regress the parameters for the rotation and the translation separately. Specifically, the rotation regression branch takes all the global features as inputs and produces a 4D vector, which represents the 3D rotation \mathbf{R} in the form of quaternion [37] $\mathbf{q} \in \mathbb{R}^4$, $\mathbf{q}^T \mathbf{q} = 1$. Meanwhile, rather than regressing the translation vector $\mathbf{t} \in \mathbb{R}^3$ directly, the translation regression branch produces two 3D vectors, which represent two saliency points of the source and the reference point clouds respectively, then calculating the difference between them as \mathbf{t} . At each iteration, the transformation $\{\mathbf{q}, \mathbf{t}\}$ is obtained as

$$\mathbf{q} = f_\theta^r(\text{cat}[\mathbf{H}_{\mathcal{X}'}^r, \mathbf{H}_{\mathcal{X}'}^t, \mathbf{H}_{\mathcal{Y}}^r, \mathbf{H}_{\mathcal{Y}}^t]) \quad \text{and} \quad \mathbf{t} = \mathbf{c}_{\mathcal{Y}} - \mathbf{c}_{\mathcal{X}'} \quad (2)$$

where

$$\mathbf{c}_{\mathcal{X}'} = f_\theta^t(\text{cat}[\mathbf{H}_{\mathcal{X}'}^r, \mathbf{H}_{\mathcal{X}'}^t, \mathbf{H}_{\mathcal{Y}}^t]) \quad \text{and} \quad \mathbf{c}_{\mathcal{Y}} = f_\theta^t(\text{cat}[\mathbf{H}_{\mathcal{Y}}^r, \mathbf{H}_{\mathcal{Y}}^t, \mathbf{H}_{\mathcal{X}'}^t]). \quad (3)$$

Here, the functions $f_\theta^r(\cdot)$ and $f_\theta^t(\cdot)$ denote the rotation and translation regression networks respectively. The vectors $\mathbf{c}_{\mathcal{X}'} \in \mathbb{R}^3$ and $\mathbf{c}_{\mathcal{Y}} \in \mathbb{R}^3$ mean the coordinates of the saliency points.

3.4 Multi-level Feature Interaction

For partial-to-partial registration, it is necessary for the mapping functions to possess partiality perception ability, which means that the feature extraction processes of the source and reference point clouds need the overall information from each other.

Point-wise Feature Interaction. In the dual branches encoder, we insert the Point-wise Feature Interaction (PFI) after multiple convolution blocks. The point-wise features of one point cloud are first aggregated by channel-wise max-pooling, then broadcasted and concatenated with the point-wise features of the other point cloud at the same level. The encoder features are then updated as

$$^{(k)}\mathbf{f}_{\mathcal{X}'} = ^{(k)}g_\theta(\text{cat}[^{(k-1)}\mathbf{f}_{\mathcal{X}'}, \text{broadcast}(\max(^{(k-1)}\mathbf{f}_{\mathcal{Y}}), N_{\mathcal{X}'})]), \quad (4)$$

where the function $^{(k)}g_\theta(\cdot)$ denotes the k -th convolution block in the encoder, and $\text{broadcast}(\mathbf{z}, N)$ denotes that repeating N times for the vector \mathbf{z} at the element-wise dimension. Note that the positions of inputs are inverted when extracting features for \mathcal{Y} with shared weights.

Global Feature Interaction. Before the regression of the transformation parameters, we further strengthen the information exchanging between the inputs by the Global Feature Interaction (GFI). The rotation and the translation features of the inputs are concatenated separately and sent into a MLP to generate the hybrid global features. The entire process is defined as

$$\mathbf{H}_{\mathcal{X}'}^r = h_\theta^r(\text{cat}[\mathbf{F}_{\mathcal{X}'}^r, \mathbf{F}_{\mathcal{Y}}^r]) \quad \text{and} \quad \mathbf{H}_{\mathcal{X}'}^t = h_\theta^t(\text{cat}[\mathbf{F}_{\mathcal{X}'}^t, \mathbf{F}_{\mathcal{Y}}^t]), \quad (5)$$

where $h_\theta^r(\cdot)$ and $h_\theta^t(\cdot)$ denote the GFI functions for the rotation and translation respectively. Note that the positions of inputs are inverted when producing features for \mathcal{Y} with shared weights.

3.5 Loss Functions

Transformation Sensitivity Loss. To modify the sensitivity of the encoder to the 3D transformation, we propose the transformation sensitivity loss, which is a variant of the more common triplet loss [38]. We follow a simple intuition: the rotation branch should be more attentive to the rotation and less attentive to the translation, and vice versa for the translation branch. Hence, we cast the features of transformed source point cloud $\mathbf{F}_{\mathcal{X}'}^r$ and $\mathbf{F}_{\mathcal{X}'}^t$ as anchor features. For the rotation, the input \mathcal{X}' is first rotated by the previous predicted quaternion \mathbf{q} to form \mathcal{X}'_r , then sent into the dual branches encoder to extract features $\mathbf{F}_{\mathcal{X}'_r}^r$ and $\mathbf{F}_{\mathcal{X}'_r}^t$. Meanwhile, using translation \mathbf{t} to alternate \mathbf{q} , we can obtain the translated point cloud \mathcal{X}'_t and its features $\mathbf{F}_{\mathcal{X}'_t}^r$ and $\mathbf{F}_{\mathcal{X}'_t}^t$ for the translation in the same way. At each iteration, the loss of transformation sensitivity loss is $\mathcal{L}_s = \mathcal{L}_s^r + \mathcal{L}_s^t$, where

$$\mathcal{L}_s^r = \max(\|\mathbf{F}_{\mathcal{X}'_r}^r - \mathbf{F}_{\mathcal{X}'_t}^r\|_2 - \|\mathbf{F}_{\mathcal{X}'_r}^r - \mathbf{F}_{\mathcal{X}'_t}^t\|_2 + \delta, \|\mathbf{F}_{\mathcal{X}'_r}^r - \mathbf{F}_{\mathcal{X}'_t}^t\|_2). \quad (6)$$

Here, $\delta = 0.01$ denotes the margin that enforced between the positive and negative pairs. The loss of translation branch \mathcal{L}_s^t is calculated with the features that output from the translation branch and exchanging the positive and negative pairs.

Point-wise Feature Dropout Loss. To avoid the case that the feature extractor only concentrates on the local geometry of the inputs, we design a point-wise feature dropout loss, which encourages the network to learn the global features from more dispersed regions of the inputs. Concretely, inspired by [39], we randomly set some of the point-wise features to zero before the max-pool layers in the encoder, and the loss \mathcal{L}_d is applied to constrain the distance between the global features that calculated before and after the dropout operation, which is defined as

$$\mathcal{L}_d = \|\mathbf{F}_{\mathcal{X}'}^r - \mathbf{F}_{\mathcal{X}'_d}^r\|_2 + \|\mathbf{F}_{\mathcal{X}'}^t - \mathbf{F}_{\mathcal{X}'_d}^t\|_2 + \|\mathbf{F}_{\mathcal{Y}}^r - \mathbf{F}_{\mathcal{Y}_d}^r\|_2 + \|\mathbf{F}_{\mathcal{Y}}^t - \mathbf{F}_{\mathcal{Y}_d}^t\|_2, \quad (7)$$

where the subscript d denotes that the features are processed by the dropout operation, and the dropout ratio is set to 0.3 in all our experiments. In addition, we notice empirically that it can relieve the over-fitting to the shape prior of the training set, which promotes the generalization.

Parameter Regression Loss. Following [24, 33], we directly measure the deviation of $\{\mathbf{q}, \mathbf{t}\}$ from the ground truth. At each iteration, the 3D transformation parameter regression loss is

$$\mathcal{L}_p = |\mathbf{q} - \mathbf{q}_{gt}| + \lambda \|\mathbf{t} - \mathbf{t}_{gt}\|_2, \quad (8)$$

where subscript gt denotes the ground-truth. We notice that using the combination of ℓ^1 and ℓ^2 distance can marginally improve the performance. Besides, the factor λ is empirically set to 4.0 in all our experiments.

Combining the terms above after N iterations, we have the weighted sum loss

$$\mathcal{L}_{total} = \frac{1}{N} \sum_{i=1}^N (\mathcal{L}_p^i + \beta \mathcal{L}_s^i + \gamma \mathcal{L}_d^i), \quad (9)$$

where the factors β and γ are set to 10^{-4} and 10^{-3} in all our experiments.

4 Experiments

In this section, we show the experimental results to demonstrate the effectiveness and efficiency of our method. We also perform ablation studies to better understand the value of our construction.

4.1 Dataset and Implementation Details

Dataset. We evaluate partial-to-partial registration on ModelNet40 [40], which includes CAD models from 40 man-made object categories. We use the processed data from [24], where the axisymmetrical categories are removed to avoid the ill-posed problem, leaving 32 categories. Each point cloud contains 2,048 points that randomly sampled from the mesh faces and normalized into a unit sphere. We denote the data that the source and the reference clouds are only sampled once from the CAD model as **once-sampled (OS)**, while sampled twice separately as **twice-sampled (TS)**. We use the official train and test split of the first 14 categories for training and validation, and the official test split of the remaining 18 categories for test. It results in 4,196 training, 1,002 validation, and

Table 1: Results on ModelNet40. For each metric, the left column *OS* denotes the results on the once-sampled data, and the right column *TS* denotes the results on the twice-sampled data. Red indicates the best performance and blue indicates the second-best result.

Method	RMSE(R)		MAE(R)		RMSE(t)		MAE(t)		Error(R)		Error(t)		
	OS	TS	OS	TS	OS	TS	OS	TS	OS	TS	OS	TS	
(a) Unseen Shapes	ICP [8]	20.036	22.840	10.912	12.147	0.1893	0.1931	0.1191	0.1217	22.232	24.654	0.2597	0.2612
	Go-ICP [14]	70.776	71.077	39.000	38.266	0.3111	0.3446	0.1807	0.1936	71.597	76.492	0.3996	0.4324
	FGR [25]	48.533	46.766	29.661	29.635	0.2920	0.3041	0.1965	0.2078	55.855	57.685	0.4068	0.4263
	PointNetLK [22]	23.866	27.482	15.070	18.627	0.2368	0.2532	0.1623	0.1778	29.374	36.947	0.3454	0.3691
	DCP [15]	12.217	11.109	9.054	8.454	0.0695	0.0851	0.0524	0.0599	7.835	9.216	0.1049	0.1259
	RPMNet [17]	1.347	2.162	0.759	1.135	0.0228	0.0267	0.0089	0.0141	1.446	2.280	0.0193	0.0300
	FMR [23]	7.642	8.033	4.823	4.999	0.1208	0.1187	0.0723	0.0726	9.210	9.741	0.1634	0.1617
	DeepGMR [19]	72.310	70.886	49.769	47.853	0.3443	0.3703	0.2462	0.2582	82.652	86.444	0.5044	0.5354
	OMNet [24]	0.771	1.384	0.277	0.542	0.0154	0.0226	0.0056	0.0093	0.561	1.118	0.0122	0.0198
	Ours	0.235	0.355	0.198	0.269	0.0038	0.0063	0.0029	0.0048	0.383	0.590	0.0066	0.0110
(b) Unseen Categories	ICP [8]	20.387	22.906	12.651	13.599	0.1887	0.1994	0.1241	0.1286	25.085	26.819	0.2626	0.2700
	Go-ICP [14]	69.747	64.455	39.646	34.017	0.3035	0.3196	0.1788	0.1888	68.329	68.920	0.3893	0.4091
	FGR [25]	46.161	41.644	27.475	26.193	0.2763	0.2872	0.1818	0.1951	49.749	51.463	0.3745	0.4003
	PointNetLK [22]	27.903	42.777	18.661	28.969	0.2525	0.3210	0.1752	0.2258	36.741	53.307	0.3671	0.4613
	DCP [15]	13.387	12.507	9.971	9.414	0.0762	0.1020	0.0570	0.0730	11.128	12.102	0.1143	0.1493
	RPMNet [17]	3.934	7.491	1.385	2.403	0.0441	0.0575	0.0150	0.0258	2.606	4.635	0.0318	0.0556
	FMR [23]	10.365	11.548	6.465	7.109	0.1301	0.1330	0.0816	0.0837	12.159	13.827	0.1773	0.1817
	DeepGMR [19]	75.773	68.425	53.689	46.269	0.3485	0.3667	0.2481	0.2595	85.210	87.192	0.5074	0.5323
	OMNet [24]	3.719	4.014	1.314	1.619	0.0392	0.0406	0.0151	0.0179	2.657	3.206	0.0321	0.0383
	Ours	1.325	1.547	1.109	1.286	0.0142	0.0180	0.0115	0.0142	2.207	2.572	0.0245	0.0311
(c) Gaussian Noise	ICP [8]	20.566	21.893	12.786	13.402	0.1917	0.1963	0.1265	0.1278	25.417	26.632	0.2667	0.2679
	Go-ICP [14]	70.417	65.402	40.303	34.988	0.3072	0.3233	0.1822	0.1929	69.175	71.054	0.3962	0.4170
	FGR [25]	49.133	46.213	31.347	30.116	0.3002	0.3034	0.2068	0.2141	56.652	58.968	0.4230	0.4364
	PointNetLK [22]	26.476	29.733	19.258	21.154	0.2542	0.2670	0.1853	0.1937	37.688	42.027	0.3831	0.3964
	DCP [15]	13.117	12.730	9.741	9.556	0.0779	0.1072	0.0591	0.0774	11.350	12.173	0.1187	0.1586
	RPMNet [17]	4.118	6.160	1.589	2.467	0.0467	0.0618	0.0175	0.0274	2.983	4.913	0.0378	0.0589
	FMR [23]	10.604	11.674	6.725	7.400	0.1300	0.1364	0.0827	0.0867	12.627	14.121	0.1788	0.1870
	DeepGMR [19]	75.257	68.560	53.470	46.579	0.3509	0.3735	0.2519	0.2654	84.121	87.104	0.5180	0.5455
	OMNet [24]	3.572	4.356	1.570	1.924	0.0391	0.0486	0.0172	0.0223	3.073	3.834	0.0359	0.0476
	Ours	1.614	1.817	1.363	1.537	0.0157	0.0197	0.0130	0.0159	2.673	3.003	0.0273	0.0341
(d) Different Partial Manner	ICP [8]	17.439	18.588	8.954	9.628	0.0848	0.0920	0.0460	0.0521	17.435	18.720	0.0905	0.1026
	Go-ICP [14]	13.081	15.214	3.617	4.650	0.0455	0.0566	0.0169	0.0223	7.184	9.002	0.0334	0.0445
	FGR [25]	19.027	33.723	8.383	19.268	0.1041	0.1593	0.0498	0.0914	15.902	35.971	0.0981	0.1828
	PointNetLK [22]	27.589	29.747	16.047	18.550	0.1516	0.1841	0.0955	0.1081	30.406	32.760	0.1907	0.1959
	DCP [15]	7.353	7.300	4.923	4.378	0.0657	0.0389	0.0451	0.0272	9.624	8.853	0.0902	0.0539
	PRNet [16]	3.241	5.883	1.632	3.037	0.0181	0.0380	0.0127	0.0237	3.095	5.974	0.0254	0.0472
	FMR [23]	4.819	5.304	2.488	2.779	0.0345	0.0323	0.0158	0.0172	4.824	5.392	0.0313	0.0342
	DeepGMR [19]	19.720	24.908	10.227	13.611	0.0915	0.1057	0.0596	0.0689	19.487	25.830	0.1188	0.1371
	IDAM [18]	5.188	8.008	3.114	4.559	0.0377	0.0484	0.0208	0.0291	5.836	8.774	0.0418	0.0578
	OMNet [24]	2.203	2.563	0.910	1.215	0.0155	0.0183	0.0078	0.0098	1.809	2.360	0.0156	0.0196
Ours	0.901	1.234	0.764	1.039	0.0062	0.0079	0.0053	0.0068	1.459	2.018	0.0107	0.0138	

1,146 test objects. Following [16, 17, 18, 24], we randomly generate three Euler angle rotations within $[0^\circ, 45^\circ]$ and translations within $[-0.5, 0.5]$ on each axis as the rigid transformation. Moreover, two different manners that proposed by [16] and [17] are applied to generate the partiality. We only report the results of the more challenging later one, please refer to our supplementary for the other.

Implementation Details. Our network structure is illustrated in Figure 1. We run $N = 4$ iterations of alignment without shared weights among different iterations. To stabilize training, the gradients of $\{\mathbf{q}, \mathbf{t}\}$ are stopped at the start of each iteration. We train the network using Adam [41] optimizer with a learning rate 0.0001. The batch size is set to 64, and training for 260k steps.

4.2 Baseline Algorithms

We compare our method to traditional methods: ICP [8], Go-ICP [14], FGR [25], and recent learning-based works: PointNetLK [22], DCP [15], RPMNet [17], FMR [23], PRNet [16], IDAM [18], DeepGMR [19] and OMNet [24]. We use implementations of ICP and FGR in Intel Open3D [42] and official implementations of the others released by their authors. Note that the normals used in FGR and RPMNet are calculated after data pre-processing, and FMR is trained with supervising.

For consistency with [16, 17, 18], we measure root mean squared error (RMSE), mean absolute error (MAE), and the isotropic error (Error). Angular measurements are in units of degrees. All metrics should be zero if the rigid alignment is perfect.

Table 2: Ablation studies of each component. SB: single branch, DB: dual branches, SP: saliency points regression, TSL: transformation sensitivity loss, PFDL: point-wise feature dropout loss. The best results are marked in bold.

	PFI	GFI	SB	DB	SP	TSL	PFDL	RMSE(R)	MAE(R)	RMSE(t)	MAE(t)	Error(R)	Error(t)
1)			✓					2.810	2.370	0.0319	0.0261	4.652	0.0552
2)	✓		✓					2.237	1.891	0.0256	0.0206	3.710	0.0443
3)		✓	✓					2.578	2.175	0.0290	0.0236	4.276	0.0503
4)	✓	✓	✓					2.288	1.899	0.0258	0.0209	3.807	0.0446
5)				✓				2.930	2.462	0.0318	0.0257	4.842	0.0551
6)				✓	✓			2.719	2.258	0.0282	0.0231	4.699	0.0512
7)	✓			✓	✓			2.303	1.925	0.0253	0.0205	3.824	0.0438
8)		✓		✓	✓			2.147	1.809	0.0229	0.0184	3.551	0.0396
9)	✓	✓		✓	✓			1.919	1.605	0.0214	0.0173	3.183	0.0370
10)	✓	✓		✓	✓	✓		1.855	1.574	0.0205	0.0165	3.091	0.0356
11)	✓	✓		✓	✓	✓	✓	1.817	1.537	0.0197	0.0159	3.003	0.0341

4.3 Evaluation on ModelNet40

Unseen Objects. We first train and test the models on the training and test sets of the same categories. Note that the source and the reference point clouds of the *TS* data have no exact correspondences in each other. Table 1(a) shows the results, where our method ranks first in all measures. A qualitative comparison of the registration results can be found in Figure 2(a).

Unseen Categories. To evaluate the generalization ability, we train the models on the first 14 categories and test on the test set of the remaining unseen categories. The results are summarized in Table 1(b). It can be found that all the learning-based methods consistently perform worse without training on the same categories. However, the traditional algorithms are not affected so much because that the handcrafted features are not sensitive to the shape variance. Our method outperforms its competitors in all metrics. A qualitative example of registration can be found in Figure 2(b).

Gaussian Noise. In this experiment, we evaluate the robustness to noise, which is always presented in real-world point clouds. We test on the unseen categories and add random noise that independently sampled from $\mathcal{N}(0, 0.01^2)$ and clipped to $[-0.05, 0.05]$ for each point. As shown in Table 1(c), FGR is more sensitive to noise, so that it performs much worse than the noise-free case. All learning-based methods get worse with noises injected. Our method exhibits the best robustness compared to the others. An example result on noisy data is shown in Figure 2(c).

Different Partial Manner. To demonstrate the effectiveness to different partiality, we further test all the algorithms on the unseen categories used the partial manner in [17]. We retrain the learning-based methods and the results are shown in Table 1(d). Our method shows robustness to the partiality, and achieves stronger performance than the others.

4.4 Ablation Studies

We perform ablation studies to demonstrate the effectiveness of each component in our method. All studies in this section are evaluated on the unseen categories with noise.

Dual Branches Structure. The dual branches (DB) structure is an important feature of our network. Here, we replace it with a single branch (SB) structure, where the feature encoder and regression network for the rotation and translation are shared weights. Comparing the first and the fifth rows in Table 2, simply applying the DB structure brings no performance gain, since the information of the rotation and translation is still hybrid without additional supervising. However, only the DB structure can enable the ability of learning attentive features, so as to further enhance the feature interaction.

Multi-level Feature Interaction. The multi-level feature interaction is another important aspect that should be studied. Therefore, we compare the performances in the case of with and without the PFI and GFI respectively. Comparing the first four rows in Table 2, we can see that only the PFI improves the performance with a large margin. Since the same encoder is applied for the rotation and the translation in the SB structure, it may confuse the GFI with their information blended. However, comparing the sixth to ninth rows in Table 2, both the PFI and the GFI improve the performance in our DB structure, and it achieves extra improvement by combining them.

Table 3: Speed comparison for registering a point cloud pair of various sizes (in milliseconds). The missing result in the table is due to the limitation in GPU memory.

# points	ICP [8]	FGR [25]	PointNetLK [22]	DCP [15]	PRNet [16]	FMR [23]	RPMNet [17]	IDAM [18]	DeepGMR [19]	OMNet [24]	Ours
512	33	37	73	15	79	138	58	27	9	24	15
1024	56	92	77	17	84	158	115	28	9	25	15
2048	107	237	83	26	114	295	271	33	9	27	15
4096	271	673	89	88	-	764	726	62	10	32	15

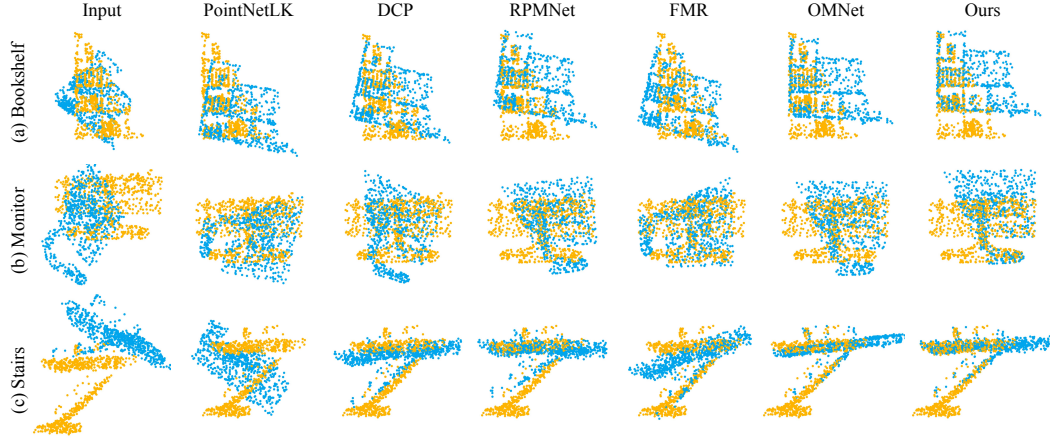


Figure 2: Qualitative examples on (a) Unseen objects, (b) Unseen categories, and (c) Gaussian noise.

Transformation Sensitivity Loss. We exam the effectiveness of our Transformation Sensitivity Loss (TSL) by comparing the performance in the case of with and without it. Comparing the ninth and tenth rows in Table 2, it improves the performance with the TSL supervising. This supports the intuition that registration becomes more precise with the rotation and translation branches more attentive to themselves and less attentive to each other, and it exists space difference between them.

Point-wise Feature Dropout Loss. We also study the significance of our Point-wise Feature Dropout Loss (PFDL) by ablating it. Comparing the last two rows in Table 2, the PFDL can marginally improves the performance on the test set. In addition, we notice that the network converges more rapidly with the PFDL supervising.

4.5 Efficiency

We test the inference time of all the methods except Go-ICP, which is obviously slower than the others. The experiment is run on a GeForce RTX 2080 Ti with 2 Intel Xeon Gold 6130 CPUs and 32GB RAM. As shown in Table 3, we test the speed on the inputs with 512, 1024, 2048, 4096 points. Our method is insensitive to the number of points, but is slightly slower than the non-iterative DeepGMR.

4.6 Robustness Against Noise

In this experiment, we further test the robustness against noise by evaluating our model on the unseen categories of the ModelNet40 dataset under different noise levels. As shown in Figure 3, the noises are sampled from $N(0, \sigma^2)$ and clipped to $[-0.05, 0.05]$, where the deviation $\sigma \in [0.02, 0.05]$. Our model achieves comparable performance under various noise levels, which supports the conclusion that our method is insensitive to the noise.

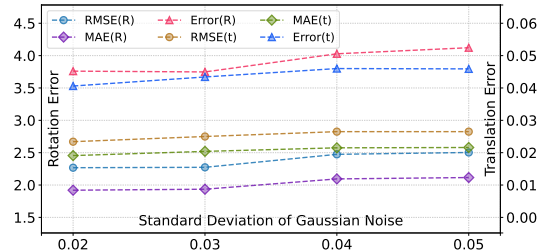


Figure 3: Errors under different noise levels.

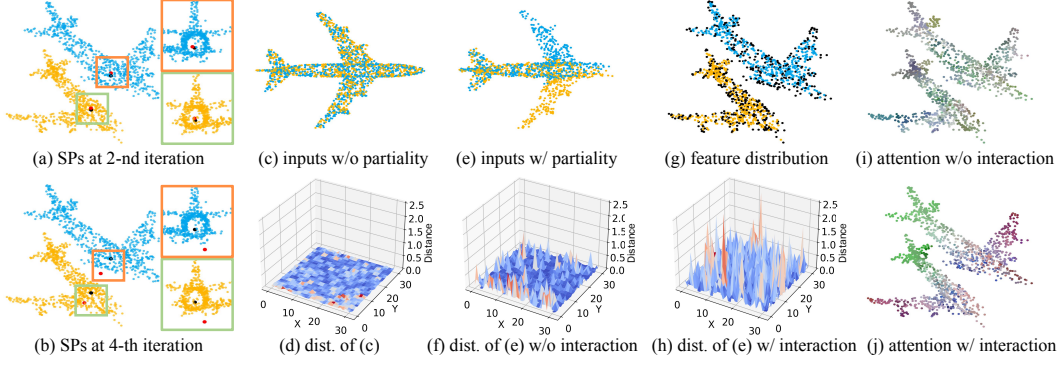


Figure 4: Visualization results in §5.1 and §5.2. SP denotes saliency point and dist. means distance.

5 Discussion

5.1 Translation Regression: Distance or Saliency Points?

We first try to answer why estimating the saliency points (SP) is better. Theoretically, directly regressing the translation implements two steps implicitly: (1) estimate the SP for the inputs; (2) compute the difference between them as translation, which can be described as

$$\mathbf{R}\mathbf{c}_{\mathcal{X}} + \mathbf{t} = \mathbf{c}_{\mathcal{Y}}, \quad \text{where} \quad \begin{cases} \mathbf{R} \neq \mathbf{E} & \text{requires } \mathbf{R}\mathbf{c}_{\mathcal{X}} = \mathbf{c}_{\mathcal{X}} \\ \mathbf{R} \approx \mathbf{E} & \text{requires } \mathbf{c}_{\mathcal{X}} \text{ corresponds to } \mathbf{c}_{\mathcal{Y}} \end{cases} \Rightarrow \mathbf{t} = \mathbf{c}_{\mathcal{Y}} - \mathbf{c}_{\mathcal{X}}. \quad (10)$$

Here, it requires that $\mathbf{c}_{\mathcal{X}}$ is the rotation center when \mathbf{R} is not approximately equal to the identity matrix \mathbf{E} , otherwise $\mathbf{c}_{\mathcal{X}}$ only needs corresponding to $\mathbf{c}_{\mathcal{Y}}$. Comparing the fifth and sixth rows in Table 2, saliency points regression can improve the performance, which supports the intuition that the optimization of the regression network can benefit from the more explicit goal. We visualize the rotation centers and the predicted SPs in black and red respectively after the second and last iteration, as shown in Figure 4(a-b). The predicted SPs close to the rotation center when it exists a rotation gap between the inputs, otherwise merely form the correspondences.

5.2 Partiality Perception Ability

To explore the partiality perceptual ability of our method. We first calculate the distances between the global features of the inputs in three cases. We can see that it tries to extract the same features for the inputs without the feature interaction, which is however perturbed by the partiality, as shown in Figure 4(f). In contrast to the intuition that concentrating on the overlapping regions, the network seems to learn how to utilize the partiality information to better register with the feature interaction, resulting in the larger distance between the global features, as shown in Figure 4(h).

Moreover, we also visualize where the values in global feature come from when utilizing the feature interaction, and the source points are shown in black. As shown in Figure 4(g), some of the non-overlapping points also have contributions, which supports the above conjecture. Finally, we show the attentive areas of the global features with and without the feature interaction, where the colors denote different iterations, as shown in Figure 4(i-j). Interestingly, with the data association, the network tends to focus on distinct areas at each iteration. In contrast, the areas are almost the same without the feature interaction, which reflects the lack of partiality perception.

6 Conclusion

We present the FINet, an end-to-end global feature-based algorithm for adapting data association for the partial-to-partial point cloud registration. Our method possesses the multi-level feature interaction based on a dual branches structure, which enables early information exchange between the inputs. In addition, we design a transformation sensitivity loss and a point-wise feature dropout loss to learn attentive and distinctive features for the rotation and the translation respectively. Experimental results show the state-of-the-art performance and robustness of our method.

References

- [1] Ronald T Azuma. A survey of augmented reality. *Presence: Teleoperators & Virtual Environments*, 6(4):355–385, 1997.
- [2] Julie Carmigniani, Borko Furht, Marco Anisetti, Paolo Ceravolo, Ernesto Damiani, and Misa Ivkovic. Augmented reality technologies, systems and applications. *Multimedia Tools and Applications*, 51(1):341–377, 2011.
- [3] Mark Billinghurst, Adrian Clark, and Gun Lee. A survey of augmented reality. *Interaction*, 8(2-3):73–272, 2014.
- [4] Eric Brachmann, Alexander Krull, Frank Michel, Stefan Gumhold, Jamie Shotton, and Carsten Rother. Learning 6d object pose estimation using 3d object coordinates. In *Proc. ECCV*, pages 536–551, 2014.
- [5] Chen Wang, Danfei Xu, Yuke Zhu, Roberto Martín-Martín, Cewu Lu, Li Fei-Fei, and Silvio Savarese. Densefusion: 6d object pose estimation by iterative dense fusion. In *Proc. CVPR*, pages 3343–3352, 2019.
- [6] Shahram Izadi, David Kim, Otmar Hilliges, David Molyneaux, Richard Newcombe, Pushmeet Kohli, Jamie Shotton, Steve Hodges, Dustin Freeman, Andrew Davison, et al. Kinectfusion: Real-time 3d reconstruction and interaction using a moving depth camera. In *Annual ACM Symposium on User Interface Software and Technology*, pages 559–568, 2011.
- [7] Michael Merickel. 3d reconstruction: the registration problem. *Computer vision, Graphics, and Image Processing*, 42(2):206–219, 1988.
- [8] Paul J. Besl and Neil D. McKay. A method for registration of 3d shapes. volume 14, pages 239–256, 1992.
- [9] Szymon Rusinkiewicz and Marc Levoy. Efficient variants of the icp algorithm. In *International Conference on 3-D Digital Imaging and Modeling (3DIM)*, pages 145–152, 2001.
- [10] Andrew W. Fitzgibbon. Robust registration of 2d and 3d point sets. *Image and Vision Computing*, 21(13-14):1145–1153, 2003.
- [11] Aleksandr Segal, Dirk Haehnel, and Sebastian Thrun. Generalized-icp. In *Robotics: Science and Systems*, volume 2, page 435, 2009.
- [12] Sofien Bouaziz, Andrea Tagliasacchi, and Mark Pauly. Sparse iterative closest point. In *Computer Graphics forum*, volume 32, pages 113–123, 2013.
- [13] François Pomerleau, Francis Colas, and Roland Siegwart. A review of point cloud registration algorithms for mobile robotics. *Foundations and Trends in Robotics*, 4(1):1–104, 2015.
- [14] Jiaolong Yang, Hongdong Li, and Yunde Jia. Go-icp: Solving 3d registration efficiently and globally optimally. In *Proc. CVPR*, pages 1457–1464, 2013.
- [15] Yue Wang and Justin M. Solomon. Deep closest point: Learning representations for point cloud registration. In *Proc. ICCV*, pages 3523–3532, 2019.
- [16] Yue Wang and Justin M. Solomon. Prnet: Self-supervised learning for partial-to-partial registration. In *Proc. NeurIPS*, pages 8814–8826, 2019.
- [17] Zi Jian Yew and Gim Hee Lee. Rpm-net: Robust point matching using learned features. In *Proc. CVPR*, pages 11824–11833, 2020.
- [18] Jiahao Li, Changhao Zhang, Ziyao Xu, Hangning Zhou, and Chi Zhang. Iterative distance-aware similarity matrix convolution with mutual-supervised point elimination for efficient point cloud registration. In *Proc. ECCV*, pages 378–394, 2020.
- [19] Wentao Yuan, Benjamin Eckart, Kihwan Kim, Varun Jampani, Dieter Fox, and Jan Kautz. Deepgmr: Learning latent gaussian mixture models for registration. In *Proc. ECCV*, pages 733–750, 2020.
- [20] Yue Wang, Yongbin Sun, Ziwei Liu, Sanjay E. Sarma, Michael M. Bronstein, and Justin M. Solomon. Dynamic graph CNN for learning on point clouds. *ACM Trans. Graphics*, 38(5):1–12, 2019.
- [21] Ashish Vaswani, Noam Shazeer, Niki Parmar, Jakob Uszkoreit, Llion Jones, Aidan N Gomez, Łukasz Kaiser, and Illia Polosukhin. Attention is all you need. In *Proc. NeurIPS*, pages 5998–6008. 2017.

- [22] Yasuhiro Aoki, Hunter Goforth, Rangaprasad Arun Srivatsan, and Simon Lucey. PointNetLK: Robust & efficient point cloud registration using pointnet. In *Proc. CVPR*, pages 7163–7172, 2019.
- [23] Xiaoshui Huang, Guofeng Mei, and Jian Zhang. Feature-metric registration: A fast semi-supervised approach for robust point cloud registration without correspondences. In *Proc. CVPR*, pages 11366–11374, 2020.
- [24] Hao Xu, Shuaicheng Liu, Guangfu Wang, Guanghui Liu, and Bing Zeng. Omnet: Learning overlapping mask for partial-to-partial point cloud registration. *arXiv preprint arXiv:2103.00937*, 2021.
- [25] Qian-Yi Zhou, Jaesik Park, and Vladlen Koltun. Fast global registration. In *Proc. ECCV*, pages 766–782, 2016.
- [26] Radu Bogdan Rusu, Nico Blodow, and Michael Beetz. Fast point feature histograms (FPFH) for 3d registration. In *IEEE International Conference on Robotics and Automation (ICRA)*, pages 3212–3217, 2009.
- [27] Charles R. Qi, Hao Su, Kaichun Mo, and Leonidas J Guibas. Pointnet: Deep learning on point sets for 3d classification and segmentation. In *Proc. CVPR*, pages 652–660, 2017.
- [28] Charles R. Qi, Li Yi, Hao Su, and Leonidas J Guibas. Pointnet++: Deep hierarchical feature learning on point sets in a metric space. In *Proc. NeurIPS*, pages 5099–5108, 2017.
- [29] Zi Jian Yew and Gim Hee Lee. 3dfeat-net: Weakly supervised local 3d features for point cloud registration. In *Proc. ECCV*, pages 630–646, 2018.
- [30] Jiaxin Li and Gim Hee Lee. Usip: Unsupervised stable interest point detection from 3d point clouds. In *Proc. ICCV*, pages 361–370, 2019.
- [31] Martin A. Fischler and Robert C. Bolles. Random sample consensus: a paradigm for model fitting with applications to image analysis and automated cartography. *Communications of the ACM*, 24(6):381–395, 1981.
- [32] Bruce D. Lucas and Takeo Kanade. An iterative image registration technique with an application to stereo vision. In *Proc. IJCAI*, page 674–679, 1981.
- [33] Vinit Sarode, Xueqian Li, Hunter Goforth, Yasuhiro Aoki, Rangaprasad Arun Srivatsan, Simon Lucey, and Howie Choset. Pcnnet: Point cloud registration network using pointnet encoding. *arXiv preprint arXiv:1908.07906*, 2019.
- [34] Eric Jang, Shixiang Gu, and Ben Poole. Categorical reparameterization with gumbel-softmax. *arXiv preprint arXiv:1611.01144*, 2016.
- [35] Richard Sinkhorn. A relationship between arbitrary positive matrices and doubly stochastic matrices. *The Annals of Mathematical Statistics*, 35(2):876–879, 1964.
- [36] Zitian Huang, Yikuan Yu, Jiawen Xu, Feng Ni, and Xinyi Le. Pf-net: Point fractal network for 3d point cloud completion. In *Proc. CVPR*, pages 7662–7670, 2020.
- [37] Ken Shoemake. Animating rotation with quaternion curves. In *Annual Conference on Computer Graphics and Interactive Techniques*, pages 245–254, 1985.
- [38] Xingping Dong and Jianbing Shen. Triplet loss in siamese network for object tracking. In *Proc. ECCV*, pages 459–474, 2018.
- [39] Pierre Baldi and Peter J Sadowski. Understanding dropout. In *Proc. NeurIPS*, pages 2814–2822, 2013.
- [40] Zhirong Wu, Shuran Song, Aditya Khosla, Fisher Yu, Linguang Zhang, Xiaoou Tang, and Jianxiong Xiao. 3d ShapeNets: A deep representation for volumetric shapes. In *Proc. CVPR*, pages 1912–1920, 2015.
- [41] P. Diederik Kingma and Lei Jimmy Ba. Adam: A method for stochastic optimization. In *Proc. ICLR*, 2015.
- [42] Qian-Yi Zhou, Jaesik Park, and Vladlen Koltun. Open3d: A modern library for 3d data processing. *arXiv preprint arXiv:1801.09847*, 2018.

A Overview

This supplementary material provides more details on experiments in the main paper and includes more experiments to validate and analyze our proposed method. In §B, we describe details in two data generation manners for point cloud registration, which are proposed by PRNet [16] and RPMNet [17] separately. In §C, we show more experimental results including the performance on the validation and the test sets, which are generated by the above two data generation manners.

B Details in Experiments

In this section, we describe two strategies to sample point clouds from the CAD models in §B.1. Then, we describe two different manners to generate the partial-to-partial point cloud pairs. One of them proposed by RPMNet [17] is detailed in §B.2, and the other used in PRNet [16] is described in §B.3. Figure 5 illustrates some examples of the data, which show the difference between them.

B.1 Point Cloud Sample Strategies

We apply two different strategies to sample the point clouds from the CAD models. Most of the previous works use processed data from PointNet [27], which only contains 2,048 points sampled from the CAD model for each object. We denote this sample strategy as once-sampled (*OS*). However, in the realistic scene, the points in the source point cloud \mathcal{X} have no exact correspondences in the reference point cloud \mathcal{Y} . Recently, OMNet [24] solves this issue by randomly sampling the point clouds 40 times from the CAD model for each object. Then, the input pair \mathcal{X} and \mathcal{Y} are randomly chosen from these 40 point clouds each time during training. We denote this sample strategy as twice-sampled (*TS*). To have an institute realization, we show the difference between the *OS* and the *TS* data in Figure 5(a-b). For consistency with the previous methods, we evaluate and compare the performances on the datasets generated by these two sample strategies.

B.2 Data Generation Manner of RPMNet

We use this manner to generate data for the first three experiments (Unseen Objects, Unseen Categories, and Gaussian Noise) in our main paper. We use the same approach as which is used in RPMNet [17] to obtain the inputs. For each point cloud, we sample a half-space with a random direction, and shift it such that approximately 70% of the points are retained. Then, the point clouds are randomly sampled to 717 points. We obtain 3D rotation by sampling three Euler angle rotations in the range $[0^\circ, 45^\circ]$ and 3D translation in the range $[-0.5, 0.5]$ on each axis. The rigid transformation is applied to \mathcal{X} , leading to \mathcal{Y} . We show some examples in Figure 5(d). The points in \mathcal{X} and \mathcal{Y} are more decentralized than those generated in the manner of PRNet [16], which means that the overlapping ratio is small in some cases. As a result, it is more difficult to register with this data.

B.3 Data Generation Manner of PRNet

We use this manner to generate data for the last experiment (Different Partial Manner) in our main paper. We use the same approach as which is used in PRNet [16] to obtain the inputs. The 3D rotation along each axis is sampled in $[0^\circ, 45^\circ]$ and the 3D translation is in $[-0.5, 0.5]$. The rigid transformation is applied to \mathcal{Y} , leading to \mathcal{X} . After that, we simulate the partial inputs by randomly placing a point in space and computing its 768 nearest neighbors in \mathcal{X} and \mathcal{Y} respectively. We show some examples in Figure 5(c). The point clouds \mathcal{X} and \mathcal{Y} are similar in most of cases, which means that the overlapping ratio is large.

C More Experimental Results

In this section, we provide more experimental results on ModelNet40 [40] and Stanford 3D Scan [?] datasets to further validate the robustness and effectiveness of our method.

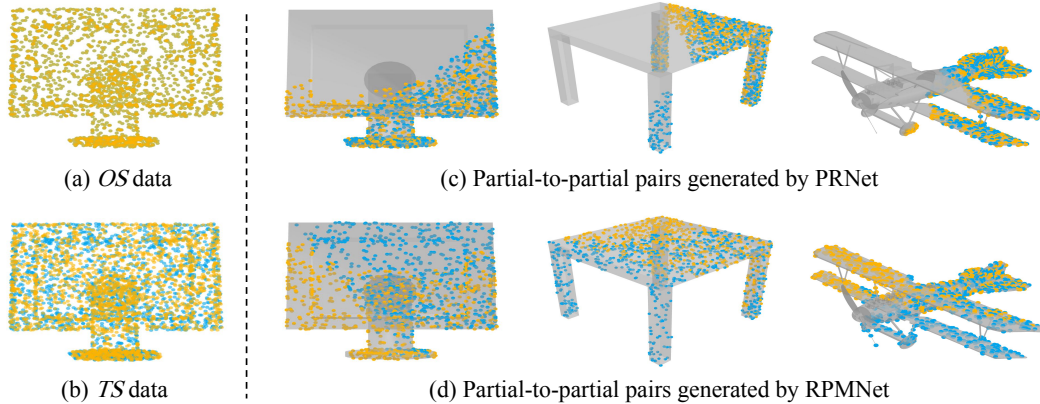


Figure 5: The difference between the *OS* and the *TS* data, and the difference between the partial-to-partial pairs that generated by PRNet and RPMNet.

C.1 More Results on RPMNet Dataset

In our main paper, we only show the results on unseen categories with Gaussian noise, which is generated in the data generation manner of RPMNet [17]. To further demonstrate the robustness of our method, we report the results on the unseen objects with Gaussian noise, which is sampled from $\mathcal{N}(0, 0.01^2)$ and clipped to $[-0.05, 0.05]$ on each axis. As shown in Table 4(a), our method achieves accurate registration and ranks first in all metrics.

C.2 More Results on PRNet Dataset

In this subsection, we alternate the data generation manner with that used in PRNet [16] on the ModelNet40 dataset, and repeat all the above-mentioned experiments.

Unseen Objects. In this experiment, we train and test the models on the training and test sets of the first 14 categories. Table 4(b) shows the results. We can find that all traditional methods and most of the learning-based methods perform poorly due to the large difference in initial positions and partiality. Note that the normal is computed after the data pre-processing, so that the normal of points in \mathcal{X} can be different from their correspondences in \mathcal{Y} . Our method outperforms all traditional and learning-based methods by a large margin.

Unseen Categories. We test the performance on the unseen categories in this experiment. The models are trained on the first 14 categories and tested on the other 18 categories. The results are summarized in Table 4(c). We can find that the performances of all learning-based methods become worse without training on the same categories. Nevertheless, traditional registration algorithms are not affected so much because of the handcrafted features. Our method outperforms the others in all metrics.

Gaussian Noise. Since we have shown the experimental results on the unseen categories with Gaussian noise in our main paper, we only report the performances on the unseen objects with noise injected here, as shown in Table 4(d). FGR [25] is sensitive to noise, so that it performs much worse than the noise-free case. Almost all of the learning-based methods become worse with noise injected. Our method achieves the best performance compared to all competitors.

C.3 Results on Stanford 3D Scan Dataset

We test our method on the Stanford 3D Scan [?] dataset. We use the partial manner of PRNet to generate partial-to-partial data. Both the source and the reference point clouds are sampled from the original CAD models separately. To demonstrate the generalization ability of our model, we directly use our model that only trained on the ModelNet40 dataset. The results are shown in Figure 6.

Table 4: More Results on ModelNet40 dataset. For each metric, the left column *OS* denotes the results on the once-sampled data, and the right column *TS* denotes the results on the twice-sampled data. Red indicates the best performance and blue indicates the second-best result. † and ‡ denote the results on the data that generated in the manners of RPMNet [17] and PRNet [16] respectively.

	Method	RMSE(R)		MAE(R)		RMSE(t)		MAE(t)		Error(R)		Error(t)	
		OS	TS	OS	TS	OS	TS	OS	TS	OS	TS	OS	TS
(a) Gaussian Noise †	ICP [8]	20.245	23.174	11.134	12.405	0.1902	0.1932	0.1214	0.1231	22.580	25.147	0.2634	0.2639
	Go-ICP [14]	72.221	72.030	40.516	39.308	0.3162	0.3468	0.1860	0.1977	74.420	77.519	0.4089	0.4405
	FGR [25]	53.186	47.816	33.189	30.572	0.3059	0.3149	0.2117	0.2185	63.019	59.759	0.4368	0.4459
	PointNetLK [22]	24.162	26.235	16.222	17.874	0.2369	0.2582	0.1684	0.1805	32.108	36.109	0.3555	0.3771
	DCP [15]	12.387	12.393	9.147	9.534	0.0656	0.1008	0.0495	0.0717	8.341	8.955	0.0989	0.1516
	RPMNet [17]	1.670	2.955	0.889	1.374	0.0310	0.0360	0.0111	0.0163	1.692	2.746	0.0242	0.0353
	FMR [23]	8.026	8.591	5.051	5.303	0.1244	0.1249	0.0755	0.0776	9.657	10.383	0.1702	0.1719
	DeepGMR [19]	74.958	70.810	52.119	47.954	0.3520	0.3689	0.2538	0.2597	86.935	87.444	0.5189	0.5360
	OMNet [24]	0.998	1.522	0.555	0.817	0.0172	0.0189	0.0078	0.0098	1.078	1.622	0.0167	0.0208
	Ours	0.431	0.625	0.369	0.517	0.0055	0.0084	0.0045	0.0068	0.699	1.023	0.0096	0.0145
(b) Unseen Shapes ‡	ICP [8]	21.043	21.246	8.464	9.431	0.0913	0.0975	0.0467	0.0519	16.460	17.625	0.0921	0.1030
	Go-ICP [14]	13.458	11.296	3.176	3.480	0.0462	0.0571	0.0149	0.0206	6.163	7.138	0.0299	0.0407
	FGR [25]	4.741	28.865	1.110	16.168	0.0269	0.1380	0.0070	0.0774	2.152	30.192	0.0136	0.1530
	PointNetLK [22]	16.429	14.888	7.467	7.603	0.0832	0.0842	0.0443	0.0464	14.324	14.742	0.0880	0.0920
	DCP [15]	4.291	5.786	3.006	3.872	0.0426	0.0602	0.0291	0.0388	5.871	7.903	0.0589	0.0794
	PRNet [16]	1.588	3.677	0.976	2.201	0.0146	0.0307	0.0101	0.0204	1.871	4.223	0.0201	0.0406
	FMR [23]	2.740	3.456	1.448	1.736	0.0250	0.0292	0.0112	0.0138	2.793	3.281	0.0218	0.0272
	DeepGMR [19]	13.266	21.985	6.883	11.113	0.0748	0.0936	0.0476	0.0587	13.536	20.806	0.0937	0.1171
	IDAM [18]	4.744	7.456	1.346	4.387	0.0395	0.0604	0.0108	0.0352	2.610	8.577	0.0216	0.0698
	OMNet [24]	0.898	1.045	0.325	0.507	0.0078	0.0084	0.0049	0.0056	0.639	0.991	0.0099	0.0112
Ours	0.092	0.496	0.078	0.422	0.0008	0.0038	0.0007	0.0033	0.148	0.797	0.0013	0.0066	
(c) Unseen Categories ‡	ICP [8]	17.236	18.458	8.610	9.335	0.0817	0.0915	0.0434	0.0505	16.824	18.194	0.0855	0.0993
	Go-ICP [14]	13.572	14.162	3.416	4.190	0.0448	0.0533	0.0152	0.0206	6.688	8.286	0.0299	0.0409
	FGR [25]	6.390	29.838	1.240	16.361	0.0375	0.1470	0.0081	0.0818	2.204	31.153	0.0156	0.1630
	PointNetLK [22]	18.294	21.041	9.730	10.740	0.0917	0.1130	0.0526	0.0629	18.845	20.438	0.1042	0.1250
	DCP [15]	6.754	7.683	4.366	4.747	0.0612	0.0675	0.0403	0.0427	8.566	9.764	0.0807	0.0862
	PRNet [16]	2.712	6.506	1.372	3.472	0.0171	0.0388	0.0118	0.0257	2.607	6.789	0.0237	0.0510
	FMR [23]	5.041	5.119	2.304	2.349	0.0383	0.0296	0.0158	0.0147	4.525	4.553	0.0314	0.0292
	DeepGMR [19]	18.890	23.472	9.322	12.863	0.0870	0.0987	0.0559	0.0658	17.513	24.425	0.1108	0.1298
	IDAM [18]	6.852	8.346	1.761	4.540	0.0540	0.0590	0.0138	0.0329	3.433	8.679	0.0275	0.0656
	OMNet [24]	2.079	2.514	0.619	1.004	0.0177	0.0147	0.0077	0.0078	1.241	1.949	0.0154	0.0154
Ours	0.438	1.271	0.373	1.065	0.0031	0.0067	0.0027	0.0058	0.709	2.083	0.0054	0.0117	
(d) Gaussian Noise ‡	ICP [8]	19.945	21.265	8.546	9.918	0.0898	0.0966	0.0482	0.0541	16.599	18.540	0.0949	0.1070
	Go-ICP [14]	13.612	12.337	3.655	3.880	0.0489	0.0560	0.0174	0.0218	7.257	7.779	0.0348	0.0433
	FGR [25]	22.347	34.035	10.309	19.188	0.1070	0.1601	0.0537	0.0942	19.934	35.775	0.1068	0.1850
	PointNetLK [22]	20.131	22.399	11.864	13.716	0.0972	0.1092	0.0516	0.0601	18.552	20.250	0.1032	0.1291
	DCP [15]	4.862	4.775	3.433	2.964	0.0486	0.0474	0.0340	0.0300	6.653	6.024	0.0690	0.0616
	PRNet [16]	1.911	3.197	1.213	2.047	0.0180	0.0294	0.0123	0.0195	2.284	3.932	0.0245	0.0392
	FMR [23]	2.898	3.551	1.747	2.178	0.0246	0.0273	0.0133	0.0155	3.398	4.200	0.0260	0.0307
	DeepGMR [19]	17.693	20.433	8.578	10.964	0.0849	0.0944	0.0531	0.0593	16.504	20.830	0.1048	0.1183
	IDAM [18]	5.551	6.846	2.990	3.997	0.0486	0.0563	0.0241	0.0318	5.741	7.810	0.0480	0.0629
	OMNet [24]	1.009	1.305	0.548	0.757	0.0089	0.0103	0.0061	0.0075	1.076	1.490	0.0123	0.0149
Ours	0.504	0.666	0.439	0.573	0.0038	0.0050	0.0033	0.0043	0.798	1.064	0.0066	0.0087	

C.4 Number of Iterations

The model is trained with different iterations to show that how many iterations are needed. We show the results on the unseen objects and the unseen categories, as illustrated in Figure 7. We can find that the most performance gains are in the first two iterations, and we choose $N = 4$ for the trade-off between the speed and the accuracy in all experiments.

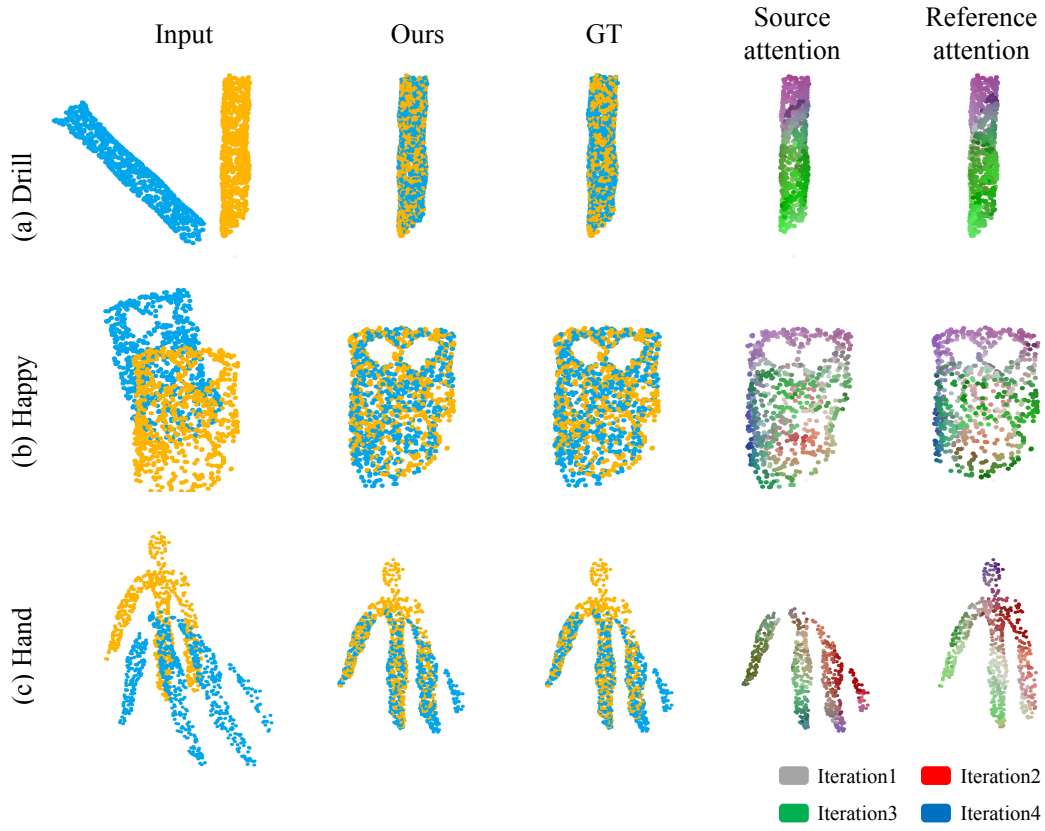


Figure 6: Qualitative examples on Stanford 3D Scan dataset without fine-tuning.

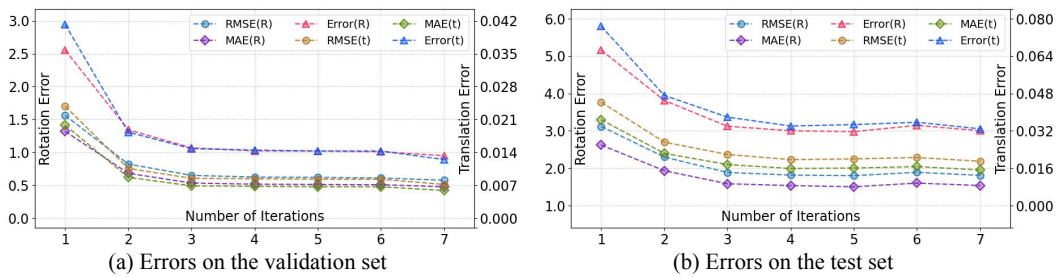


Figure 7: Evaluation on the validation and the test sets of ModelNet40 dataset.